# Quantifying variability in radiation dose due to respiratory-induced tumor motion

S.E. Geneser [a,\*], J.D. Hinkle [a], R.M. Kirby [a], B. Wang [b], B. Salter [b], S. Joshi [a]

[a] *Scientific Computing & Imaging Institute, University of Utah, Salt Lake City, UT, USA*
[b] *Huntsman Cancer Institute, University of Utah, Salt Lake City, UT, USA*

## ARTICLE INFO

## ABSTRACT

State of the art radiation treatment methods such as hypo-fractionated stereotactic body radiation therapy (SBRT) can successfully destroy tumor cells and avoid damaging healthy tissue by delivering high-level radiation dose that precisely conforms to the tumor shape. Though these methods work well for stationary tumors, SBRT dose delivery is particularly susceptible to organ motion, and few techniques capable of resolving and compensating for respiratory-induced organ motion have reached clinical practice. The current treatment pipeline cannot accurately predict nor account for respiratory-induced motion in the abdomen that may result in significant displacement of target lesions during the breathing cycle. Sensitivity of dose deposition to respiratory-induced organ motion represents a significant challenge and may account for observed discrepancies between predictive treatment plan indicators and clinical patient outcomes.

Improved treatment-planning and delivery of SBRT requires an accurate prediction of dose deposition uncertainties resulting from respiratory motion. To accomplish this goal, we developed a framework that models both organ displacement in response to respiration and the underlying random variations in patient-specific breathing patterns. Our organ deformation model is a four-dimensional maximum a *posteriori* (MAP) estimation of tissue deformation as a function of chest wall amplitudes computed from clinically obtained respiratory-correlated computed tomography (RCCT) images. We characterize patient-specific respiration as the probability density function (PDF) of chest wall amplitudes and model patient breathing patterns as a random process. We then combine the patient-specific organ motion and stochastic breathing models to calculate the resulting variability in radiation dose accumulation. This process allows us to predict uncertainties in dose delivery in the presence of organ motion and identify tissues at risk of receiving insufficient or harmful levels of radiation.

## 1. Introduction

External beam radiotherapy destroys cancer cells by delivering ionizing radiation to a tumor. Because conventional radiation treatment delivers only a few unmodulated straight-line beams per treatment, the volume receiving radiation cannot be easily matched to the irregular shape of most tumors. Modern techniques like dynamic conformal arc and intensity modulated radiation therapy (IMRT) modulate the intensity or shape of external beams applied over many different angles to enable radiation dose delivery that precisely conforms to a physician-defined tumor geometry (Purdy, 2001). Combined with improved image guidance techniques that allow clinicians to identify tumor shapes and locations with greater accuracy (Xing et al., 2006), IMRT enables precise dose conformity to the targeted tumor volume (as demonstrated in Fig. 1). This process allows safe delivery of extremely large ablative radiation doses that dramatically increases the likelihood of tumor control (Timmerman et al., 2005) and reduces the collateral damage to surrounding healthy tissue, particularly in cases where the tumor is stationary during treatment. Hypo-fractionated stereotactic body radiation therapy (SBRT) combines conformal therapy and image guidance techniques to apply high levels of radiation over a few treatments (each treatment delivers a fraction of the total prescribed dose) and has proven safe and highly effective for controlling tumors of the lung, liver, and spine (McGarry et al., 2005).

State-of-the-art commercial treatment-planning systems generally calculate dose delivery distributions for static tissues within 3% accuracy (Siantar et al., 2001; Heath et al., 2004; Herk, 2004; Rassiah-Szegedi et al., 2006), but cannot yet calculate accurate dose in the presence of organ motion. Though respiratory-induced organ motion can result in significant movement during the breathing cycle (Lujan et al., 1999; Brandner et al., 2006) (as evidenced in Fig. 2), clinical radiation dose SBRT plans deliver dose to a static volume over all treatments and do not dynamically adjust to changing tumor position. Due to high dose gradients inherent in conformal radiation delivery, IMRT is particularly

\* Corresponding author. Present address: Department of Radiation Oncology, Stanford University, Stanford, CA, USA.
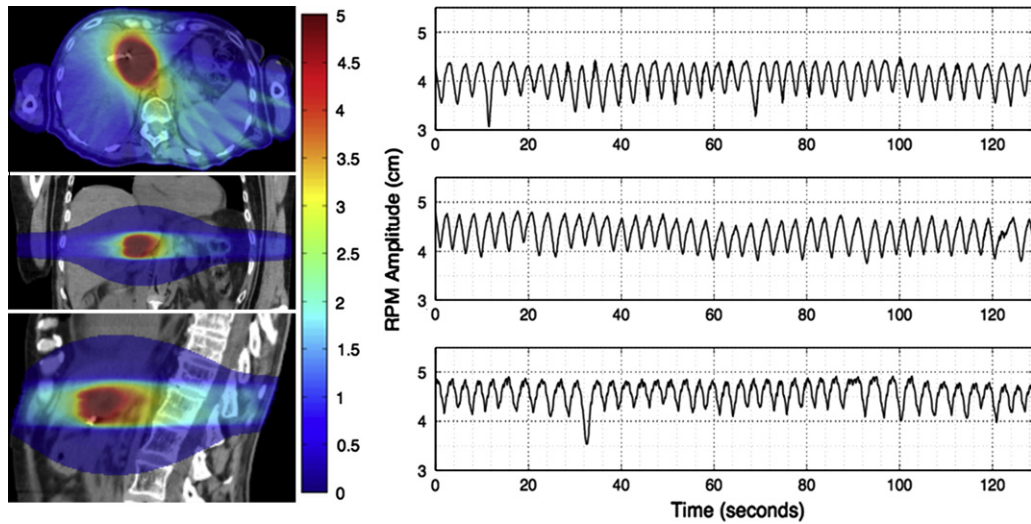*E-mail address:* sgeneser@stanford.edu (S.E. Geneser).

**Fig. 1.** *The planned (static) dose distribution and Real-time Position Management™ (RPM) traces* for the analyzed SBRT liver cancer patient illustrates the high spatial gradients of target-conforming dose and daily variations in breathing. The static deposited dose (in units of Gray) is color-mapped and superimposed on anatomical images for (from top to bottom) axial, sagittal, and coronal views. The RPM breathing traces are recorded for the same patient and time interval on different treatment days.
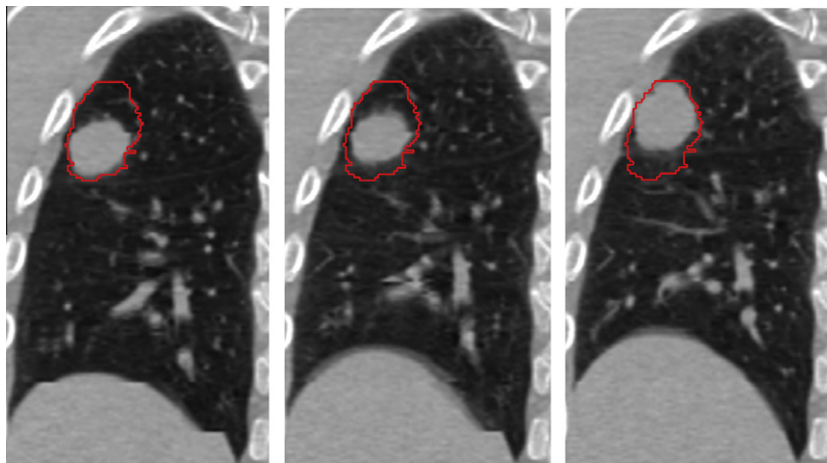


**Fig. 2.** *Respiratory-induced organ motion* can cause significant tumor displacement. These coronal slices depict recorded anatomy corresponding to three phases (from left to right: full-inhale, mid-cycle, and full-exhale) within the breathing cycle for a typical lung SBRT patient. The red outline denotes the physician defined internal target volume (ITV). Note the displacement of the tumor within the (stationary) clinical ITV. (For interpretation of the references to color in this figure legend, the reader is referred to the web version of this article.)

susceptible to targeted tumor motion and respiration can lead to significant dose delivery errors (Bortfeld et al., 2002; Lujan et al., 2003; Chui et al., 2003; Jiang et al., 2003; Bortfeld et al., 2004; Vedam et al., 2005). The low number of treatment fractions renders SBRT even more sensitive to intra-fraction motion and studies investigating the dosimetric consequences of respiratory-induced tissue motion on SBRT have found variations between planned and delivered dose distributions as significant as 20% (Wu et al., 2008). The uncertainties resulting from respiratory-induced tissue motion complicate SBRT treatment of extracranial lesions and may well account for the observed discrepancies between predictive indicators and clinical patient outcome statistics. No process has been developed to accurately predict uncertainties in dose delivery resulting from random patient breathing patterns.

Controlling patient breathing during treatment and restricting beam-on times to windows of low variation in patient anatomy can reduce the variability in dose deposition due to respiratory-induced motion. Specific methods to reduce dose variation include respiratory-gating (Keall et al., 2005b), breath-hold (Hanley et al., 1996), and coached breathing (Neicu et al., 2006). However, each has limitations and none are appropriate for all patients (Keall et al., 2006). For example, breath-hold techniques can induce an unacceptable level of patient discomfort (particularly for lung cancer patients with severely compromised respiratory function), respiratory-gating significantly increases the treatment time because it restricts beam delivery to a small fraction of the treatment period, and coached breathing may be impractical because some patients are not trainable. While some radiation oncologists employ these methods, most instead design a treatment based on more fundamental mechanisms, e.g., the inclusion of a border or margin around the defined internal target volume (ITV). This widely employed technique is intended to accommodate tumor motion during treatment and ensure sufficient dose delivery by treating a "motion envelope" that encompasses the tumor positions observed during breathing. However, tumor volumes and margins for treatment-planning are generated from images ob-

tained on a single day that cannot be used to predict the subsequent variations in breathing. Moreover, this approach ensures a complete treatment of the target at the expense of irradiating adjacent healthy tissues. Alternative treatment methods have been developed that adjust to or move with the tumor in order to accommodate respiratory-motion. Such methods are successful in some cases but cannot yet be widely applied. For example, automated tumor tracking and delivery (Keall et al., 2004; Naqvi et al., 2005; Sawant et al., 2008) works well for lung tumors that are clearly discernible in CT and X-ray images, but typically not for liver, which can be difficult to distinguish from surrounding tissue. As a result, it is challenging to implement robust and accurate automatic tracking methods for liver tumors. For thorax and abdominal tumors, breathing motion remains one of the major obstacles to reducing the irradiation volume while maintaining a high probability of treatment success (Jiang et al., 2008).

Patient breathing is not time-periodic (or perfectly repeatable), and respiration patterns can vary significantly between treatment fractions. The fundamentally random fluctuations in respiratory-induced organ motion can result in delivered doses that significantly vary from treatment to treatment. Failure to accommodate patient breathing motion randomness can result in under-dosing of the target and/or deposition of potentially dangerous dose levels to surrounding healthy tissue. When limiting patient organ motion during treatment is impossible or unreasonable, it is essential to incorporate an accurate prediction of the effects of the stochastic respiratory process on dose deposition for improved safety and efficacy of SBRT treatment-planning and delivery. Though several groups have worked to develop accurate models that incorporate the effect of respiratory-induced organ motion on dose deposition (Boldea et al., 2008), no commercially available computational tools successfully address this problem. We propose an approach capable of predicting the variance in dose accumulation for SBRT treated abdominal lesions resulting from stochastic organ motion induced by variations in patient breathing patterns.

We apply our framework (described previously in Geneser et al. (2009)) to quantify the impact of variations in patient-specific breathing patterns on dose deposition for a typical SBRT liver patient. The anatomical CT images, clinical dose plans, and forward dose calculations used in this work were obtained during the Huntsman Cancer Institute's clinical planning and treatment process. The patient's static dose treatment plan and breathing traces from three treatment days are depicted in Fig. 1. We provide a flow chart (depicted in Fig. 3) to outline the major components of our

procedure and indicate how the clinical data is incorporated into our framework. While the results presented here are a retrospective analysis, the same approach can be applied to predict dose uncertainties on a patient-specific basis prior to treatment with minimal alteration of the clinical planning routine. Because the anatomical CT images are collected and dose distributions are calculated as part of a typical SBRT dose planning process, our framework requires only that breathing traces be obtained on a few days prior to treatment. This can be accomplished without extending the planning time because the dose optimization process currently requires several days of computation time during which the breathing traces can be recorded and analyzed.

To predict the variability in radiation dose delivery resulting from random patient breathing patterns, we build a model of patient-specific respiratory-induced organ motion to compute the dynamic dose deposition in response to recorded breathing behavior during a given treatment using the method described in Hinkle et al. (2009). We then model patient-specific breathing patterns as a stochastic process by parametrizing the recorded breathing traces and modelling the resulting breathing parameters as random variables. Once we estimate the underlying distributions of the random variables, we incorporate our stochastic breathing model into the dynamic dose computation that accounts for variations in organ motion during treatment.

Monte Carlo techniques cannot be employed to solve such systems because the large number of solutions necessary to converge to accurate statistics and long computational times required to generate a single dynamic dose solution renders such methods infeasible. Using polynomial chaos (Wiener, 1938; Xiu and Karniadakis, 2002) and Smolyak collocation (Mathelin and Hussaini, 2003; Babuška et al., 2005; Xiu and Hesthaven, 2005; Xiu, 2007; Ganapathysubramanian and Zabaras, 2007; Nobile et al., 2008) techniques significantly reduces the number of dynamic dose calculations and thus the cost of computing accurate dose statistics. Indeed, the speedup is significant enough to render incorporating the framework into the clinical optimization and planning process feasible. Using this method, we compute pertinent dose statistics to predict and assess variations in radiation dose due to random variations in patient breathing patterns subsequent to the clinical planning process. Our goal is to enable clinicians to identify SBRT dose plans that are robust to fluctuations in patient respiratory patterns and improve tumor control and normal tissue sparing.

## 2. Methods

To account for stochastic respiratory-induced tumor motion, we first quantify the impact of organ motion on dose delivery over the course of a treatment. Calculating the dynamic dose requires both an accurate patient-specific anatomical motion model and the ability to calculate static dose deposition at anatomical configurations observed during unrestricted patient breathing. Commercially available four-dimensional respiratory-correlated computed tomography (4D RCCT) (Ford et al., 2003; Vedam et al., 2003) tools provide a means of visualizing four-dimensional organ motion, and clinicians currently rely on the detailed images produced from such scans to generate the volume contours to be irradiated. Using deformable image registration techniques, the anatomical CT configurations observed during the breathing cycle can be mapped onto a common geometry. This mapping can be used to compute the dynamic dose accumulation resulting from observed or simulated respiratory-induced tissue deformations (Foskey et al., 2005; Keall et al., 2005a).

We build an explicit model of tissue deformation from anatomical CT patient images obtained during the breathing cycle. Our motion model and subsequent dose calculations rely on the well-
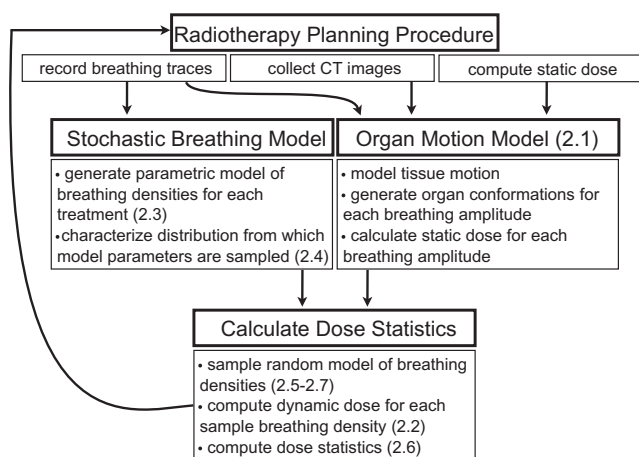


**Fig. 3.** *Overview* of the procedure for calculating variations in radiation dose resulting from fluctuations in respiratory-induced organ motion. Where appropriate, the sections describing the components are denoted.

justified and widely accepted assumption that the anatomical configuration is a function of breathing pattern as measured by a surrogate signal, e.g., the real-time position management (RPM™) system (Kubo et al., 2000) (Varian RPM, Varian Medical Systems Inc., Palo Alto, CA). Several groups have investigated the relationship between external and internal motion markers (Beddar et al., 2007; Ionascu et al., 2007) and reported high correlation between the two. This correspondence is the basis for the respiratory-correlated spiral CT (RCCT) method that generates CT images at multiple respiratory phases from a single spiral CT scan (Ford et al., 2003; Vedam et al., 2003).

From the patient images, we construct a deformation field, $h(\vec{x}, a(t))$, that maps each spatial point, $\vec{x}$, in a base image to its corresponding anatomical position as a function of breathing amplitude. Generating deformation fields that model organ motion is a well-studied problem and several groups have developed techniques that produce accurate deformations from artifact-free CT images (Pevsner et al., 2006; Wijesooriya et al., 2008). We model the three-dimensional tissue motion as a function of breathing amplitude rather than phase. Several groups have shown that organ position correlates highly with breathing amplitude (Nehmeh et al., 2004; Chi et al., 2006; Abdelnour et al., 2007). In the following sections, we describe our methods to construct a set of amplitude-indexed deformations which represent the fully deformable diffeomorphic transformation of a base image in response to breathing motion.

## 2.1. Four-dimensional geometric model of organ deformation

To construct a physiologically realistic model of organ motion, we follow the 4D maximum a posteriori (MAP) image reconstruction approach proposed by Hinkle et al. (2009) that estimates amplitude-varying velocity fields acting on the tissue during breathing from 4D RCCT images. Rather than calculating correspondences between pairs of binned images, this method simultaneously estimates deformations and the base organ configuration over the entire set of collected CT data. In contrast, binning methods discard a significant amount of the CT data and can result in image artifacts due to mismatched slices. In this framework, one estimates a 4D time-indexed image, $I_t(\vec{x})$, by maximizing a posterior likelihood that combines prior motion information with a data log-likelihood term derived from a noise model.

The raw data are modeled as a set of projections, $d_i \in L^2(\Omega_d)$, obtained via linear operators $P_i : L^2(\Omega) \rightarrow L^2(\Omega_d)$, where $\Omega \subset \mathbb{R}^3$ is the image domain, and $\Omega_d$ is the data domain. In this notation, $L^2(X)$ denotes the Hilbert space of square-integrable functions over the domain, $X$, equipped with the usual inner product. For cone-beam CT, the projection operator is the conebeam projection and $\Omega_d \subset \mathbb{R}^2$ is two-dimensional because the detector consists of a two-dimensional array of elements. In the case of fan beam images, the data domain, $\Omega_d \subset \mathbb{R}^1$, is one-dimensional and the operator is given by the Radon transform. Because organ motion is considerably slower than RCCT gantry rotation, we reconstruct each slice assuming no anatomical motion and $P_i$ becomes a simple slice selection operator.

Deriving an expression for the data log-likelihood requires a model of the noise characteristics of the scanner. For CT data with sufficiently high signal-to-noise ratio, the noise is approximately Gaussian, and the data log-likelihood is a sum of squared differences between the projected image estimate and the data as follows:

$$L(\{d_i\}|I_t) = \frac{1}{2\sigma^2} \sum_{i=1}^{N} \int_{s \in \Omega_d} |P_i\{I_{t_i}\}(s) - d_i(s)|^2 ds. \tag{1}$$

It is worth noting that interpreting Eq. (1) as a log-likelihood function is non-trivial. Extending the notion of a normal distribution to

the infinite-dimensional Hilbert space, $L^2(\Omega)$, in a rigorous way is possible but requires careful treatment of stochastic processes and Gaussian random fields. For a more in-depth discussion of these issues see Christensen et al. (1996) and Dupuis et al. (1998).

We model the 4D image, $I_t(\vec{x}) = I_0 \circ g(\vec{x}, t)$, as a 3D base image, $I_0$, undergoing a time-indexed deformation, $g(\vec{x}, t)$. Assuming organ motion is correlated with breathing amplitude, the deformations are amplitude-indexed as $h(\vec{x}, a(t))$. The velocity of a point, $\vec{x}$, in the patient's anatomy is described by the ordinary differential equation,

$$\frac{d}{dt}h(\vec{x}, a(t)) = v(h(\vec{x}, a(t)), a(t))\frac{da}{dt}, \tag{2}$$

where $v(h(a, \vec{x}), a) = \frac{\partial}{\partial a}h(\vec{x}, a)$ is a velocity field indexed by breathing amplitude rather than time. The deformation from the base amplitude is given by the associated integral equation,

$$h(\vec{x}, a) = \vec{x} + \int_0^a v(h(\vec{x}, a'), a')da'. \tag{3}$$

This formulation guarantees that the resulting estimates of patient anatomy are diffeomorphic to one another and ensures that organs do not tear or disappear during breathing (Joshi et al., 2000). Diffeomorphic deformations also provide a one-to-one correspondence between image points, which enables tissue trajectory tracking. We enforce smoothness by introducing a prior on the velocities via a Sobolev norm, $\|v\|_V^2$, defined by:

$$\|v\|_V^2 = \langle v, v \rangle_V = \int_0^1 \int_{\vec{x} \in \Omega} \|Lv(\vec{x}, a)\|_{\mathbb{R}^3}^2 d\vec{x} da, \tag{4}$$

where $L$ is a differential operator chosen to reflect physical tissue properties. Following Kuo, 1975 we place a Gaussian prior on the Sobolev space, which is embedded in a Banach space of continuous vector fields. The continuity properties of elements in the Banach space are determined by the choice of Sobolev space, which in turn is determined by the choice of differential operator $L$. In our implementation, $Lv = -\alpha\nabla^2 v + \gamma v$ for scalar parameters $\alpha$ and $\gamma$, following Christensen et al. (1996, 2005).

We enforce further physical tissue properties by constraining the velocity fields. In particular, if the divergence of the velocity field is zero, the resulting deformation has unit Jacobian determinant and is locally volume preserving. This is a necessary constraint when modeling the breathing induced motion of incompressible fluid-filled organs such as liver.

Combining the data log-likelihood with the motion prior, the log-posterior likelihood of observing the data takes the form:

$$\mathscr{L}(I_0, v|d_i) = -\|v\|_V^2 - \frac{1}{2\sigma^2} \sum_i \int_{s \in \Omega_d} |P_i\{I_0 \circ h(\vec{x}, a_i)\}(s) - d_i(s)|^2 ds. \tag{5}$$

A MAP estimate that maximizes Eq. (5) with respect to both the base image and deformation is obtained via an alternating iterative algorithm that updates the deformation and image estimates at each iteration using a gradient ascent step and the associated Euler–Lagrange equation, respectively. Following the approach of Beg et al. (2005), efficient computations of the Euler–Lagrange equations are implemented in the Fourier domain, requiring only a matrix multiplication and Fourier transforms of $v_k$ at each iteration of the algorithm. We enforce the zero-divergence velocity field constraint at each step in the Fourier domain, and additional implementation details can be found in Hinkle et al. (2009).

As with the data log-likelihood term, one must be careful when interpreting Eq. (5) as a posterior likelihood. A formal prior distribution may be placed on the space of velocity fields by defining a Gaussian random field on the Sobolev space characterized by the differential operator $L$. Because probability density functions do

not exist on the infinite-dimensional spaces in which we define our probability distributions, strict interpretation of the data and prior expressions as density functions is imprecise. However, an extension of MAP estimation to infinite-dimensional posterior distributions can be made precise. In this approach densities are replaced by the limits of probabilities of balls around a given point. In the case of a Gaussian random field, the result is an expression known as the Onsager–Machlup functional, which takes the form of an exponentiated squared norm, as is the case for both the data log-likelihood and prior terms in Eq. (5). As discussed by Dupuis et al. (1998), such a treatment is quite involved, and it is often more convenient to simply view the proposed approach as a minimum-energy estimation problem.

## 2.2. Incorporating organ motion into dynamic dose calculation

The dynamic dose deposition, $D$, accounts for the effects of known organ motion during a single treatment interval and is integrated over the time interval $[0,T]$ as follows:

$$D = \int_0^T d_t(g(\vec{x},t),t)dt. \tag{6}$$

The term, $d_t(g(\vec{x},t),t)$, is the time-dependent static dose over the patient's anatomy at time $t$, $g(\vec{x},t)$. A change of variables yields the total deposited dose over a treatment period as an integral over the amplitudes,

$$D = \int_{min(a)}^{max(a)} d_a(h(\vec{x},a),a)f(a)da, \tag{7}$$

where $d_a(h(\vec{x},a),a)$ is the amplitude-dependent dose corresponding to $a(t)$, the amplitude of the breathing signal during treatment, mapped to the base image according to the deformation field, $h(\vec{x},a(t))$, and $f(a)$ is the relative time density of the breathing amplitudes over the treatment interval. Given a set of amplitude-binned CT images and a model of the organ deformation as described above, we estimate the delivered dose by discretizing Eq. (7) to obtain a weighted sum of amplitude-indexed dose images as follows:

$$D = \sum_{i=0}^N w_i d(h(a_i),a_i), w_i = \int_{a_i - \delta a}^{a_i + \delta a} f(a)da, \tag{8}$$

where $\delta a = \frac{1}{2}(a_{i+1} - a_i)$ is the size of the amplitude discretization. The term $d(h(a_i),a_i)$ is the dose deposited to the tissues at the anatomical conformation corresponding to the breathing amplitude, $a_i$. The weights, $w_i$, account for the relative amount of time the breathing amplitude falls within the interval, $[a_i - \delta a, a_i + \delta a]$, during a treatment period.

It is important to stress that the dynamic model of dose deposition presented above accounts only for the respiratory-induced organ motion observed during a single treatment. As such, it includes none of the expected variability due to patient breathing motion. For $D$ to provide insight to the effects of motion variability, one must incorporate a model of patient breathing variability into the dynamic dose deposition calculation. In the following sections, we provide the framework to characterize the stochastic nature of daily breathing patterns and apply our model to determine the resulting uncertainties in SBRT dose accumulation.

## 2.3. Parametrization of breathing amplitude density

The extent of breathing variability differs over individuals, necessitating patient-specific respiratory models to generate accurate predictions of radiation dosing resulting from random fluctuations in breathing patterns. Because the time density of breathing amplitudes is sufficient to accurately calculate a dose distribution

over a treatment interval, we need only determine the variations in amplitude density as a function of time. To characterize the distributions from which a patient's breathing amplitude density is sampled on any given day, we first parametrize breathing density by fitting each patient breathing trace to a reasonable probability distribution. Parametrization is necessary to estimate the underlying distributions from which patient-specific amplitude densities are sampled and, ultimately, to develop a model that accurately captures the random fluctuations in patient breathing patterns. Once we fit the breathing densities, we then characterize the distributions of the parameters by performing principle component analysis. In this manner, we construct a patient-specific stochastic model of breathing that can be incorporated into the dose calculation to compute variances in dose deposition.

Gaussian Mixture Models (GMMs) provide a means of parametrizing the probability density of a random process (McLachlan and Peel, 2000) and are used here to model the amplitude density of individual RPM breathing traces. Such models are convex combinations of $M$ Gaussian distributions as follows:

$$m(x, p_i, \mu_i, \sigma_i) = \sum_{i=1}^M p_i \frac{1}{\sigma_i\sqrt{2\pi}} e^{\frac{-(x-\mu_i)^2}{2\sigma_i^2}} \tag{9}$$

where $\mu_i$ and $\sigma_i$ are the mean and standard deviation of the $i$th Gaussian distribution and $p_i$ are positive weighting factors that sum to one. We fit these parameters to patient RPM breathing traces using the Expectation Maximization (EM) algorithm (Dempster et al., 1977; McLachlan and Peel, 2000) that optimizes the log-likelihood estimates of the GMM fits to the RPM breathing amplitude data. Because patients pause at inhale and exhale and the amplitudes for both are typically consistent over time, one often observes peaks in the amplitude density function at both locations. As a consequence, a two-Gaussian mixture model appears sufficient for estimating and parametrizing the amplitude density of RPM breathing traces of many patients. However, breathing patterns can differ widely among patients. For certain cases (particularly for moderate to advanced lung cancer patients with compromised and erratic respiratory status), breathing patterns may be more variable in frequency, rhythm, and depth of respiration, necessitating the use of GMMs with three or more Gaussians. The appropriate model should be chosen on a case-by-case basis. Given the parameters of the RPM amplitudes, we can analyze the characteristics of variability in the parameters for each patient and build a model to capture the patient-specific variations in daily breathing amplitude densities.

## 2.4. Model of breathing variability

After fitting breathing amplitude densities to Eq. (9), we estimate the variation of the parameters over observation days to characterize the patient's breathing fluctuations. Because it is only clinically feasible to obtain a small number of breathing traces (typically less than seven are collected per patient), it is difficult to generate accurate estimates of the underlying patient-specific distribution from which the GMM breathing parameters are sampled on any given day. It is important to note that the GMM parameters; $p_i$, $\mu_i$, and $\sigma_i$, exhibit strong correlation. For example, one often observes a consistent distance between inhale and exhale amplitudes. This results in a high correlation between $\mu_i$ over the observation days. Using principal component analysis (PCA) (Pearson, 1901) we perform a linear transformation of the GMM parameters to identify the modes of greatest variation. We then formulate the patient-specific random GMM model parameters as a function of independent and uncorrelated Gaussian random variables, $\vec{\xi} = (\xi_1, \ldots, \xi_d)$, where $d$ is the number of principal components (and thus random dimensions) necessary to accurately capture the breathing variability. The Gaussian random variables

are centered at zero and have variance corresponding to the eigenvalues, $\lambda_i$, of each PCA component. The random GMM parameters are then the multiplicative sum of the Gaussian random variables, $\vec{\xi}$, and the PCA principle components (or eigenvectors) of the GMM model parameters.

### 2.5. Variations in dose

Given a model of patient-specific variability in respiratory-induced organ motion and dose calculation, we compute statistics of the deposited dose from a single fraction. With the variation in the GMM parameters expressed in terms of the $d$-dimensional random variable, $\vec{\xi}$, we incorporate the stochastic model of breathing amplitudes into a statistical characterization of the dose distribution, $D$, resulting from variations in respiratory-induced organ motion. Because the dose distribution is a direct consequence of anatomical configuration that, in turn, is a consequence of breathing amplitude, the random dynamic dose is expressed as $D(\vec{\xi})$.

In our study, we are interested in computing statistics (e.g., mean and variance) on the stochastic dose deposition, $D(\vec{\xi})$. These quantities can help assess the impact of respiratory-induced organ motion variability on SBRT dose distributions.

### 2.6. Generalized polynomial chaos-stochastic collocation

Determining the behavior of a stochastic system requires that the random inputs of the system be mathematically characterizable stochastic processes (i.e., have a known or estimable underlying distribution). Though Monte Carlo (MC) techniques provide a straightforward means of computing statistics of random fields like $D(\vec{\xi})$, the large number of samples necessary to compute accurate statistics and the significant time to calculate a single dynamic dose deposition renders random sampling Monte Carlo infeasible for clinical use. Several approaches e.g., Latin hypercube sampling (Stein, 1987; Loh, 1996; Helton et al., 2005), the quasi-Monte Carlo method (Morokoff and Caflisch, 1995; Caflisch, 1998; Niederreiter et al., 1998), and the Markov chain Monte Carlo (MCMC) method (Gamerman, 1997; Quian et al., 2003), achieve improved convergence compared to random sampling (or brute-force) Monte Carlo. However, these approaches gain efficiency at the cost of additional restrictions, and none achieve sufficient reduction in sampling size to render computing stochastic dose tractable.

The generalized polynomial chaos-stochastic collocation (gPC-SC) method (Xiu and Hesthaven, 2005; Xiu, 2007) provides a computationally efficient and easily implemented alternative to MC sampling methods, requiring far fewer samples to calculate accurate statistics. Like MC methods, gPC-SC is a sampling method in that it does not require derivation of the stochastic approximating system nor modification of the original deterministic system. In contrast to MC, where the deterministic system (in our case, the forward dose calculation) must be computed at a very large set of randomly chosen sample values of the stochastic input process (the breathing amplitude densities) gPC-SC employs quadrature rules to minimize the number of samples necessary to integrate the stochastic process of interest over the appropriate domain and compute accurate statistics. Under assumptions of smoothness of the system with respect to inputs, which in this case equate to the recognition that the dose distributions vary smoothly as a function of the breathing signal, we gain exponential convergence in the statistical accuracy as a function of the number of dose distribution forward simulations we compute. This process yields a sequence of solutions for a small and far more computationally tractable number of specific realizations of the stochastic field. These solutions are used to obtain highly accurate estimates of the mean, variance, and higher statistical moments of the system.

The generalized polynomial chaos (gPC) method provides a means of representing stochastic processes as a linear combination of orthogonal stochastic polynomials (Xiu and Karniadakis, 2002). In our case, the GMM parameters are Gaussian distributed and can be represented exactly by two Hermite polynomials. Because dose calculation is a non-linear process with respect to the GMM parameters and patient anatomy, the resulting distribution of the dose will be non-Gaussian. Stochastic processes with arbitrary or non-Gaussian distributions are represented using weighted sums of Hermite polynomials as follows: $\vec{\xi}(\omega) = \sum_{i=0}^{N} \alpha_i H_i(\omega)$, where $\omega$ is a random variable and $\alpha_i$ is a weight obtained by projecting the stochastic process onto the $i$th Hermite polynomial.

The Hermite polynomials are given by the recurrence relation:

$$H_{i+1} = 2\omega H_i - 2i H_{i-1}$$
$$H_0 = 1$$
$$H_1 = 2x$$

The stochastic collocation approach consists of selecting a collection of points at which to sample the random field and corresponding weights that account for the underlying stochastic characteristics of the system. Each collocation point, $\vec{\xi}_i$, represents a particular breathing amplitude density for the duration of a treatment selected from the set of likely breathing patterns. We compute the dose deposition for each collocation realization, $D(\vec{\xi}_i)$, using the method described in Section 2.2.

For Gaussian distributed random variables, $\psi$, of mean zero and unit variance, the collocation points, $\psi_{i,n}$, are the roots of the $n$th Hermite polynomial and the weights, $c_{i,n}$, are given by $c_{i,n} = \frac{2^{n-1} n! \sqrt{\pi}}{n^2 (H_{n-1}(\psi_i))^2}$.

Though polynomial roots can be approximated using a root-finding method like Newton's method, it is faster to use the Golub–Welsch algorithm (Golub and Welsh, 1969) in the case of Hermite polynomials (Press et al., 1992). We obtain the roots of the $n$th-order Hermite polynomial by calculating the eigenvalues of the Jacobi matrix, $J$, composed of the recurrence relation coefficients of the Hermite polynomials, and defined as follows:

$$J_n = \begin{bmatrix} a_0 & \sqrt{b_1} & & & \\ \sqrt{b_1} & a_1 & \sqrt{b_2} & & \\ & \vdots & \vdots & & \\ & & \sqrt{b_{n-2}} & a_{n-2} & \sqrt{b_{n-1}} \\ & & & \sqrt{b_{n-1}} & a_{n-1} \end{bmatrix}. \tag{10}$$

The collocation weights, $c_n$, are equivalent to the first component of the normalized eigenvectors of the Jacobi matrix $J_n$ (Press et al., 1992). To accommodate Gaussian random variables, $\vec{\xi}$, of arbitrary mean, $\mu$, and variance, $\sigma^2$, we map the collocation points as $\vec{\xi}_i = \sigma \psi_i + \mu$. The collocation weights and points can also be extended to multiple stochastic dimensions using tensor products for lower dimensions or the Smolyak construction (Xiu and Hesthaven, 2005; Xiu, 2007) for higher dimensions. We describe the technique in the following section and clearly illustrate the computational savings in Fig. 4.

For each collocation point, $\vec{\xi}_i$, representing a particular breathing amplitude density over the course of a treatment, we calculate the corresponding dose deposition, $D(\vec{\xi}_i)$. The mean and variance of the deposited dose are calculated using the forward dose computations and the collocation weights as follows:

$$\mathbb{E}[D(\vec{\xi})] \approx \sum_{i=0}^{N} c_i D(\xi_i), \tag{11}$$

$$\mathbb{E}[(D(\vec{\xi}) - \mathbb{E}[D(\vec{\xi})])^2] \approx \sum_{i=0}^{N} c_i (D(\xi_i) - \mu(D(\vec{\xi})))^2. \tag{12}$$
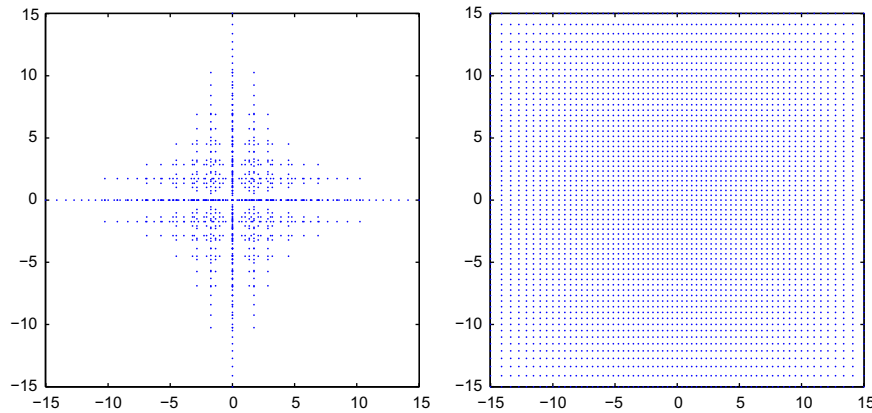
**Fig. 4.** *The two-dimensional sparse grid* interpolation nodes based on the level 5 Smolyak algorithm and Gauss–Hermite one-dimensional collocation scheme (left) requires only 837 points for the similar integration accuracy of the random process with two independent and uncorrelated Gaussian random variables as the full-tensor product algorithm (right) of the same one-dimensional nodes resulting in 4225 points.

## 2.7. Smolyak collocation points

For increasing random dimensions, the number of stochastic collocation points necessary to accurately compute integrals grows exponentially. Smolyak's construction (Smolyak, 1963) is a linear combination of one-dimensional tensor product formulas that spans a subspace of the tensor product space and requires far fewer total collocation nodes than the straightforward $d$-dimensional tensor product of one-dimensional collocation rules.

Given a one-dimensional quadrature rule,

$$Q_i(f) = \sum_{j=1}^{2i+1} c_j f(\omega_j), \tag{13}$$

where $\omega_j$ and $c_j$ are the collocation nodes and weights, respectively, the $d$-dimensional numerical approximation to the integral $\int_\Omega f(\omega) d\omega$ using Smolyak's algorithm is defined recursively as

$$Q_l^d = \sum_{i=0}^{l} (Q_i - Q_{i-1}) \otimes Q_{l-i}^{d-1} \tag{14}$$

where $Q_{-1} = 0$ and $\otimes$ denotes the tensor product of one-dimensional quadrature rules. Alternatively, we can write

$$Q_l^d = \sum_{l-d+1 \leqslant |\vec{i}| \leqslant l} (-1)^{l-|\vec{i}|} \cdot \binom{d-1}{l-|\vec{i}|} \cdot (Q_{i_1} \otimes \cdots \otimes Q_{i_d}), \tag{15}$$

where $i$ is the set of one-dimensional quadrature indices over $d$ dimensions, $l$ is the level of the Smolyak approximation, $|\vec{i}| = \sum_{k=1}^{d} i_k$, and $l \geqslant d$.

The resulting number of sparse-grid collocation points is significantly fewer than for the full-tensor construction providing an accurate cubature formula that does not suffer as significantly from the "curse of dimensionality" (Novak and Ritter, 1997) as the full-tensor construction. This computational savings is clearly illustrated in Fig. 4 which depicts both the full-tensor collocation points (4225 nodes) and the corresponding Smolyak points (837 nodes) for numerical quadrature of a process consisting of two independent and uncorrelated Gaussian random variable inputs. Because we employ three random dimensions in our model, we observe a reasonable savings in computation time with Smolyak versus tensor points. Moreover, we expect significant additional savings when increased model complexity requires the incorporation of a greater number of random dimensions.

## 3. Results

In this section, we present results for a SBRT liver cancer patient treated with four fractions in the Department of Radiation Oncology at the Huntsman Cancer Institute (HCI). Axial, sagittal, and coronal views of the patient's static dose plan and three of their representative RPM traces recorded on different days are depicted in Fig. 1. The 4DCT images used in this retrospective study were collected at HCI on a 16-slice large bore LightSpeed RT CT scanner (GE Health Care, Waukesha, WI) during the SBRT treatment process using the 4D RCCT (Ford et al., 2003; Vedam et al., 2003) scan protocol described below. Scans at each couch position were continuously acquired in the axial cine mode for a period of time equal to the maximum breathing cycle plus 1 s with a 0.5 s per revolution gantry rotation speed and slice-thickness of 1.25 mm at 120 kVp and GE software slice-thickness optimized mA. A total of roughly 2900 CT slices were acquired at 187 couch positions and the patient's breathing amplitude was continuously recorded during CT acquisition using Varian's RPM system. An additional four RPM respiratory traces were recorded during CT imaging on treatment days and all five traces were subsequently analyzed to determine the variability in patient breathing behavior. The clinical static dose calculations were performed using the BrainSCAN v5.31 (BrainLAB AG, Heimstetten, Germany) radiation treatment-planning (RTP) system's pencil beam algorithm.

Fig. 5 illustrates the two-Gaussian mixture model approximations to the amplitude densities of five recorded RPM breathing traces. Breathing amplitude histograms are depicted to provide a basis for comparing the EM fits to the breathing amplitude data. Panel (f) depicts the GMM fits and clearly illustrates the variations in the breathing amplitude density over the course of several days. Note that both the shape of the amplitude and the absolute values can change significantly. The amplitudes recorded in the first trace (Panel (a)) range from about 3.5 to 4.8 cm, while the amplitudes for the fourth RPM signal (Panel (d)) range from about 4 to 5 cm. Additionally, the qualitative shape of the second, fourth, and fifth (Panels (b), (d), and (e), respectively) GMMs differ greatly slightly from the first and significantly from the third GMMs (Panels (a) and (c), respectively). This variability differs from patient to patient and necessitates patient-specific models of breathing variability and dose delivery uncertainty.

Examination of the eigenvalues corresponding to variation in the parameters depicted in Panel (d) of Fig. 6 suggests that only three PCA components are necessary to accurately capture the variability in breathing. For visual comparison, the reconstruction of the GMM models for the five RPM breathing traces is depicted in
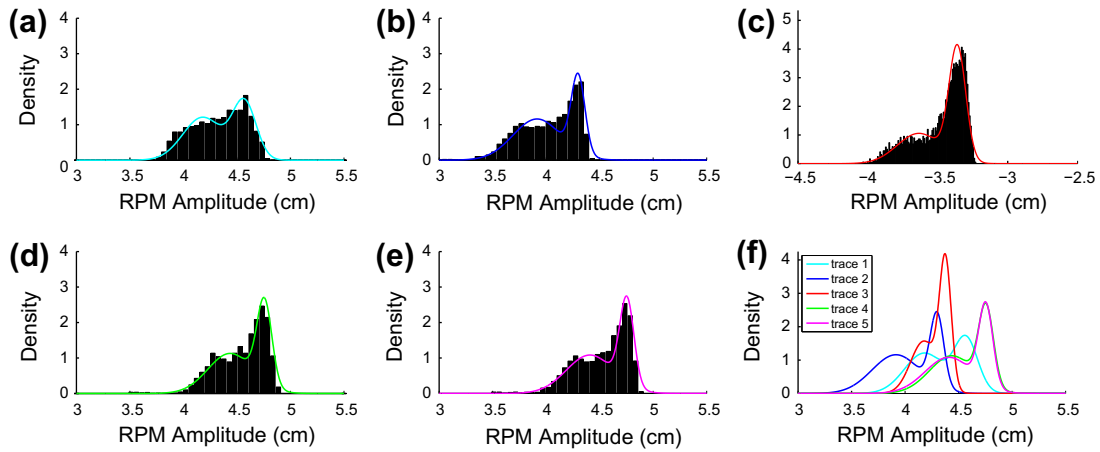
**Fig. 5.** *The Gaussian mixture model* provides an estimation of amplitude densities of the RPM breathing traces. The GMM fit for each of the five RPM traces overlays the corresponding histogram of breathing amplitudes. The daily variations in amplitude density of the different RPM traces are evident on the bottom right panel.

panels (a), (b), and (c) of Fig. 6. Though the average RMS difference between the GMMs fitted to the breathing and the reconstructed GMMs decreases from $3.8 \times 10^{-4}$ to $1.7 \times 10^{-16}$ from three to four components, the eigenvalue of the fourth principal component of the Gaussian Mixture Model parameters is quite small. The additional accuracy gained by including four rather than three components in the reconstruction is on the order of slight variations in the RPM measurement setup and, moreover, does not significantly impact the stochastic dose calculation. As such, it is not sufficient to justify the increased system complexity. The reasonably close correspondence between the original fitted and reconstructed GMMs using only three PCA components enables significant reduction in the complexity of the stochastic system owing to the correspondingly reduced dimensionality of the stochastic space. Thus,

we use three components to capture the variation observed in the breathing traces.

Fig. 7 depicts the average and standard deviations of deposited dose over a single treatment for a sagittal view. A comparison of the average dose depositions to the static dose deposition calculation in Fig. 1 shows little difference. However, examination of the standard deviation in dose shows non-trivial high values (greater than 0.2 Gray) occurring near the boundaries of the lesion. From our experiments, we have observed that large standard deviations in dose often correspond to regions of high dose gradient that undergo large respiratory-induced organ deformation. Such areas are significant because they indicate planned dose regions that may differ significantly from actual dose deposition during treatment and are likely candidates for over- or under-dosing.
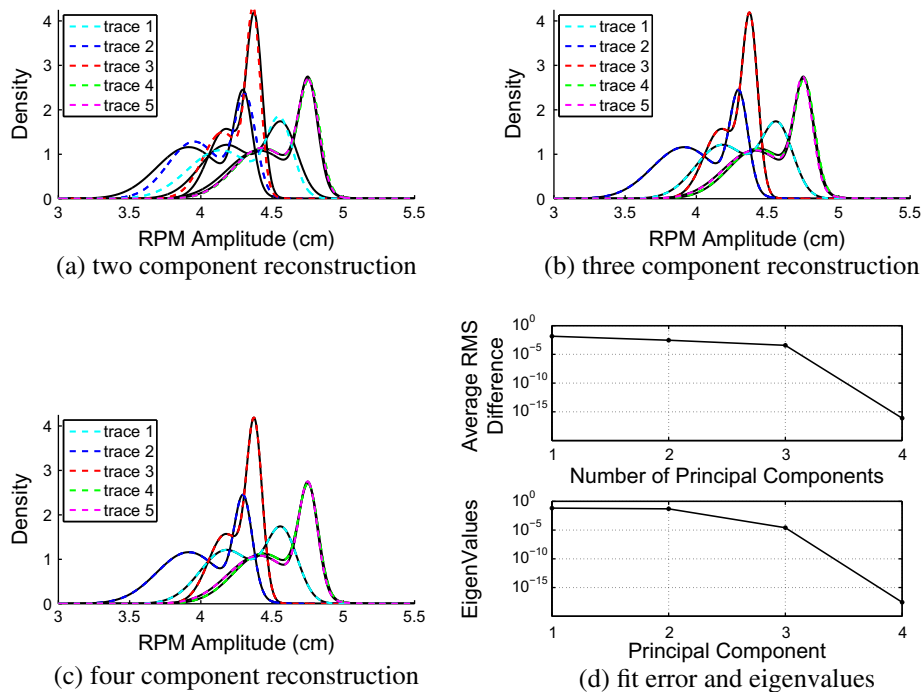


**Fig. 6.** *The reconstruction of the Gaussian mixture model fits to the breathing traces* are depicted in (a), (b), and (c) for two, three, and four component reconstructions, respectively. The reconstructions are depicted by the dashed color lines and the GMM fits to the patient breathing traces are shown in black. The principal component analysis reconstruction gives very close reproductions of the original mixture model fits with only three independent and uncorrelated eigenvectors (b). Panel (d) depicts the average root mean squared difference between the original fits and the reconstructions for different numbers of principal components in the reconstructions and the eigenvalues corresponding to each component.
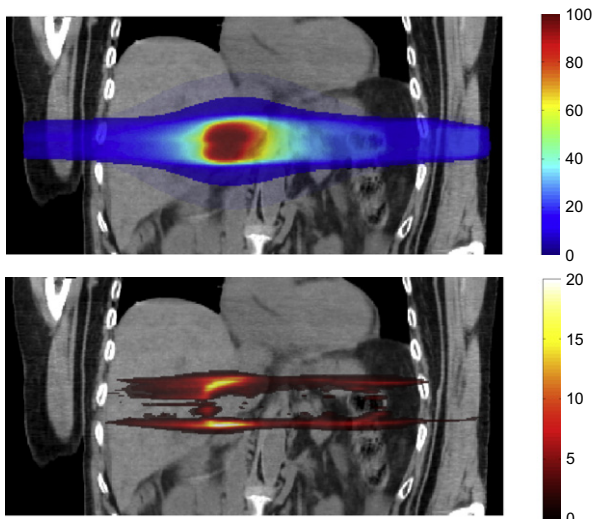
**Fig. 7.** *The average (top) and standard deviation (bottom) of stochastic dose deposition (in Gray) is depicted as a percentage of prescribed dose for coronal anatomical views.*
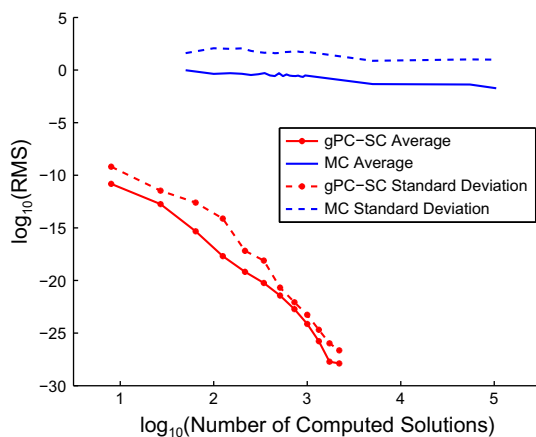


**Fig. 8.** *The convergence rates for MC and gPC-SC methods as used to compute average and standard deviation of the deposited dose.*

To validate our approach, we present in Fig. 8 the convergence in gPC-SC and traditional MC dose statistics for the patient case depicted in Fig. 7. The convergence data depicted is the RMS difference between the current and final number of forward solutions for the average and standard deviation of dose calculations. It is clear that with only 2744 realizations the gPC-SC method has reached greater convergence than the MC method with 155,000 forward dose solutions. Thus, for this particular model, gPC-SC exhibits significantly faster convergence than MC.

## 4. Discussion

The goal of this study was to demonstrate the utility and feasibility of a framework for quantifying the variability in respiratory-induced organ motion and incorporate that stochastic model into the calculation of dose deposition for SBRT treatment-planning. In contrast to Monte Carlo methods which are clinically infeasible because they require weeks or even months to compute accurate dose deposition statistics, the efficiency of the proposed approach enables physicians to perform statistical studies of dose response to breathing induced organ motion on a clinically realistic time scale. Statistical dose computations are particularly useful in plan-

ning because they allow physicians to identify and avoid dose plans in which high standard deviations in dose coincide with radiation sensitive tissues e.g., the spinal cord and cardiac tissue. We propose that accurate statistical models of predicted dose deposition resulting from organ motion will enable physicians to better assess the impact of SBRT dose plans on normal tissue and tumor lesions and reduce the tumor margins currently incorporated into the clinical SBRT treatment process.

## References

Abdelnour, A., Nehmeh, S., Pan, T., Humm, J., Vernon, P., Schröder, H., Rosenzweig, K., Mageras, G., Yorke, E., Larson, S., Erdi, Y., 2007. Phase and amplitude binning for 4D-CT imaging. Phys. Med. Biol. 52 (May), 3515–3529.

Babuška, I., Nobile, F., Tempone, R., 2005. A stochastic collocation method for elliptic partial differential equations with random input data. Tech. Rep. ICES 05-47, The University of Texas at Austin.

Beddar, A., Kainz, K., Briere, T., Tsunashima, Y., Pan, T., Prado, K., Mohan, R., Gillin, M., Krishnan, S., 2007. Correlation between internal fiducial tumor motion and external marker motion for liver tumors imaged with 4D-CT. Int. J. Radiat. Oncol. Biol. Phys. 67 (2), 630–638.

Beg, M.F., Miller, M.I., Trouvé, A., Younes, L., 2005. Computing large deformation metric mappings via geodesic flows of diffeomorphisms. Int. J. Comput. Vision 61 (2), 139–157.

Boldea, V., Sharp, G., Jiang, S., Sarrut, D., 2008. 4D-CT lung motion estimation with deformable registration: quantification of motion nonlinearity and hysteresis. Med. Phys. 35 (3), 1008–1018.

Bortfeld, T., Jokivarsi, K., Goitein, M., Kung, J., Jiang, S., 2002. Effects of intra-fraction motion on IMRT dose delivery: statistical analysis and simulation. Phys. Med. Biol. 47, 2203–2220.

Bortfeld, T., Jiang, S., Rietzel, E., 2004. Effects of motion on the total dose distribution. Semin. Radiat. Oncol. 14, 41–51.

Brandner, E., Wu, A., Chen, H., Heron, D., Kalnicki, S., Komanduri, K., Gerszten, K., Burton, S., Ahmed, I., Shou, Z., 2006. Abdominal organ motion measured using 4D CT. Int. J. Radiat. Oncol. Biol. Phys. 65, 554–560.

Caflisch, R., 1998. Monte Carlo and quasi-Monte Carlo methods. Acta Numerica, vol. 7. Cambridge University Press.

Chi, P., Balter, P., Luo, D., Mohan, R., Pan, T., 2006. Relation of external surface to internal tumor motion studied with CINE CT. Med. Phys. 33 (9), 3116–3123.

Christensen, G.E., Rabbitt, R.D., Miller, M.I., 1996. Deformable templates using large deformation kinematics. IEEE Trans. Image Process. 5 (10), 1435–1447.

Chui, C., Yorke, E., Hong, L., 2003. The effects of intra-fraction organ motion on the delivery of intensity-modulated field with a multileaf collimator. Med. Phys. 30, 1736–1746.

Dempster, A., Laird, N., Rubin, D., 1977. Maximum likelihood from incomplete data via the EM algorithm. J. Roy. Stat. Soc. B: Met. 39 (1), 1–38.

Dupuis, P., Grenander, U., Miller, M.I., 1998. Variational problems on flows of diffeomorphisms for image matching. Quart. J. Appl. Math. 56 (3), 587–600.

Ford, E., Mageras, G., Yorke, E., Ling, C., 2003. Respiration-correlated spiral CT: a method of measuring respiratory-induced anatomic motion for radiation treatment planning. Med. Phys. 30, 88–97.

Foskey, M., Davis, B., Goyal, L., Chang, S., Chaney, E., Strehl, N., Tomei, S., Rosenman, J., Joshi, S., 2005. Large deformation three-dimensional image registration in image-guided radiation therapy. Phys. Med. Biol. 50, 5869–5892.

Gamerman, L., 1997. Markov Chain Monte Carlo: Stochastic Simulation for Bayesian Inference. Chapman & Hall, London, England.

Ganapathysubramanian, B., Zabaras, N., 2007. Sparse grid collocation schemes for stochastic natural convection problems. J. Comput. Phys. 225 (1), 652–685.

Geneser, S., Kirby, R., Wang, B., Salter, B., Joshi, S., 2009. Incorporating patient breathing variations into a stochastic model of dose deposition for stereotactic body radiation therapy. Proceedings of the 21st International Conference on Information Processing in Medical Imaging, vol. 5636. Lecture Notes in Computer Science (LNCS), Williamsburg, Virginia, pp. 688–700.

Golub, G., Welsh, J., 1969. Calculation of Gauss quadrature rules. Math. Comput. 23, A1–A10.

Hanley, J., Debois, M., Raben, A., et al., 1996. Deep inspiration breath-hold technique for lung tumors: the potential value of target immobilization and reduced lung density in dose escalation. Int. J. Radiat. Oncol. Biol. Phys. 36 (1), 188.

Heath, E., Seuntjens, J., Sheikh-Bagheri, D., 2004. Dosimetric evaluation of the clinical implementation of the first commercial IMRT Monte Carlo treatment planning system at 6 MV. Med. Phys. 31, 2771–2779.

Helton, J., Davis, F., Johnson, J., 2005. A comparison of uncertainty and sensitivity analysis results obtained with random and Latin hypercube sampling. Reliab. Eng. Syst. Safe. 89, 305–330.

Herk, M.v., 2004. Errors and margins in radiotherapy. Semin. Radiat. Oncol. 14 (1), 52–64.

Hinkle, J., Fletcher, P.T., Wang, B., Salter, B., Joshi, S., 2009. 4D MAP image reconstruction incorporating organ motion. In: IPMI 2009: Proceedings of Information Processing in Medical Imaging, pp. 676–687.

Ionascu, D., Jiang, S., Nishloka, S., Shirato, H., Berbeco, R., 2007. Internal–external correlation investigations of respiratory induced motion of lung tumors. Med. Phys. 34 (10), 3893–3903.

Jiang, S., Pope, C., Al Jarrah, K., Kung, J., Bortfeld, T., Chen, G., 2003. An experimental investigation on intra-fractional organ motion effects in lung imrt treatments. Phys. Med. Biol. 48, 1773–1784.

Jiang, S., Wolfgang, J., Mageras, G., 2008. Quality assurance challenges for motion-adaptive radiation therapy: gating, breath holding, and four-dimensional computed tomography. Int. J. Radiat. Oncol. Biol. Phys. 71 (1), S103–S107.

Joshi, S.C., Miller, M.I., 2000. Landmark matching via large deformation diffeomorphisms. IEEE Trans. Image Process. 9 (8), 1357–1370.

Keall, P., Todor, A., Vedam, S., Bartee, C., Sibers, J., Kini, V., Mohan, R., 2004. On the use of EPID-based implanted marker tracking for 4D radiotherapy. Med. Phys. 31, 3492–3499.

Keall, P., Joshi, S., Vedam, S., Siebers, J., Kini, V., Mohan, R., 2005a. Four-dimensional radiotherapy planning for DMLC-based respiratory motion tracking. Med. Phys. 32, 942–951.

Keall, P., Kini, V., Vedam, S., Mohan, R., 2005b. Potential radiotherapy improvements with respiratory gating. Australas. Phys. Eng. Sci. Med. 25, 1–6.

Keall, P., Mageras, G., Balter, J., Emery, R., Forster, K., Jiang, S., Kapatoes, J., Low, D., Murphy, M., Murray, B., Ramsey, C., Van Herk, M., Vedam, S., Wong, J., Yorke, R., 2006. The management of respiratory motion in radiation oncology report of AAPM Task Group (76ª). Med. Phys. 33, 3874–3900.

Kubo, H., Len, P., Minohara, S., Mostafavi, H., 2000. Breathing-synchronized radiotherapy program at the University of California Davis Cancer Center. Med. Phys. 27 (2), 346–353.

Kuo, H.-H., 1975. Gaussian Measures in Banach Spaces. Lecture Notes in Mathematics, vol. 463. Springer-Verlag, Berlin, Heidelberg, New York.

Loh, W., 1996. On Latin hypercube sampling. Ann. Stat. 24, 2058–2080.

Lujan, A., Larsen, E., Balter, J., Ten Haken, R., 1999. A method for incorporating organ motion due to breathing into 3D dose calculations. Med. Phys. 26 (5), 715–720.

Lujan, A., Larsen, E., Balter, J., Ten Haken, R., 2003. A method for incorporating organ motion due to breathing into 3D dose calculations: sensitivity to variations in motion. Med. Phys. 10, 2643–2649.

Mathelin, L., Hussaini, M., 2003. A stochastic collocation algorithm for uncertainty analysis. Tech. Rep. NASA/CR-2003-212153, NASA Langley Research Center.

McGarry, R., Papiez, L., Williams, M., Whitofrd, T., Timmerman, R., 2005. Stereotactic body radiation therapy of early-stage non-small-cell lung carcinoma: phase I study. Int. J. Radiat. Oncol. Biol. Phys. 64, 1010–1015.

McLachlan, G., Peel, D., 2000. Finite Mixture Models. John Wiley & Sons, Inc., New York, NY.

Morokoff, W., Caflisch, R., 1995. Quasi-Monte Carlo integration. J. Cell Physiol. 122 (2), 218–230.

Naqvi, S.A., D'Souza, W.D., Yu, C., 2005. Real-time intra-fraction-motion tracking using the treatment couch: a feasibility study. Phys. Med. Biol. 50, 4021–4033.

Nehmeh, S., Erdi, Y., Pan, T., Yorke, E., Mageras, G., Rosenzweig, K., Schoder, H., Mostafavi, H., Squire, O., Pevsner, A., et al., 2004. Quantitation of respiratory motion during 4D-PET/CT acquisition. Med. Phys. 31, 1333–1338.

Neicu, T., Berbeco, R., Wolfgang, J., Jiang, S., 2006. Synchonized moving aperture radiation therapy (SMART): improvement of breathing pattern reproducibility using respiratory coaching. Phys. Med. Biol. 51, 617–636.

Niederreiter, H., Hellakalek, P., Larcher, G., Zinterhof, P., 1998. Monte Carlo and Quasi-Monte Carlo Methods. Springer-Verlag, New York, NY.

Nobile, F., Tempone, R., Webster, C., 2008. A sparse grid stochastic collocation method for partial differential equations with random input data. SIAM J. Numer. Anal. 46 (5), 2309–2345.

Novak, E., Ritter, K., 1997. The curse of dimension and a universal method for numerical integration. In: Nurnberger, G., Schmidt, J., Walz, G. (Eds.), Multivariate Approximation and Splines, pp. 177–187.

Pearson, K., 1901. On lines and planes of closest fit to systems of points in space. Philos. Mag. 2 (6), 559–572.

Pevsner, A., Davis, B., Joshi, S., et al., 2006. Evaluation of an automated deformable image matching method for quantifying lung motion in respiration-correlated CT images. Med. Phys. 33 (2), 369–376.

Press, W., Teukolsky, S., Vetterling, W., Flannery, B., 1992. Numerical Recipes in C: The Art of Scientific Computing, second ed. Cambridge University Press, New York, NY (Chapter: Gaussian Quadratures and Orthogonal Polynomials, pp. 147–161).

Purdy, J., 2001. Intensity-modulated radiotherapy: current status and issues of interest. Int. J. Radiat. Oncol. Biol. Phys. 51 (4), 880–914.

Quian, S., Stow, C., Borsuk, M., 2003. On Monte Carlo methods for Bayesian inference. Ecol. Modell. 159, 269–277.

Rassiah-Szegedi, P., Salter, B., Fuller, C., Blough, M., Papanikolaou, N., Fuss, M., 2006. Monte Carlo characterization of target doses in stereotactic body radiation therapy (SBRT). Acta Oncol. 45, 989–994.

Sawant, A., Venkat, R., Srivastava, V., Carlson, D., 2008. Management of three-dimensional intrafraction motion through real-time DMLC tracking. Med. Phys. 35 (5), 2050–2061.

Siantar, C.H., Walling, R., Daly, T., Faddegon, B., Albright, N., Bergstrom, P., et al., 2001. Description and dosimetric verification of the PEREGRINE Monte Carlo dose calculation system for photon beams incident on a water phantom. Med. Phys. 28, 122–1337.

Smolyak, S., 1963. Quadrature and interpolation formulas for tensor products of certain classes of functions. Soviet Math. Dokl. 4, 240–243.

Stein, M., 1987. Large sample properties of simulations using Latin hypercube sampling. Technometrics 29, 143–151.

Timmerman, R., Forster, K., Chinsoo, C., 2005. Extracranial stereotactic radiation delivery. Semin. Radiat. Oncol. 15, 202–207.

Vedam, S., Keall, P., Kini, V., Mostafavi, H., Shukla, H., Mohan, R., 2003. Acquiring a four-dimensional computed tomography dataset using an external respiratory signal. Phys. Med. Biol. 48 (1), 45–62.

Vedam, S., Docef, A., Fix, M., Purphy, M., Keall, P., 2005. Dosimetric impact of geometric errors due to respiratory motion prediction on dynamic multileaf collimator-based four-dimensional radiation delivery. Med. Phys. 32, 1607–1620.

Wiener, N., 1938. The homogeneous chaos. Am. J. Math. 60 (4), 897–936.

Wijesooriya, K., Weiss, E., Dill, V., Dong, L., Mohan, R., Joshi, S., 2008. Quantifying the accuracy of automated structure segmentation in 4D CT images using a deformable image registration algorithm. Med. Phys. 35 (4), 1251–1260.

Wu, Q., Thongphiew, D., Wang, Z., Chankong, V., Yin, F., 2008. The impact of respiratory motion and treatment technique on stereotactic body radiation therapy for liver cancer. Med. Phys. 35 (4), 1440–1451.

Xing, L., Thorndyke, B., Schreibmann, E., Yang, Y., Li, T., Kim, G., Luxton, G., Koong, A., 2006. Overview of image-guided radiation therapy. Med. Dosim. 31 (2), 91–112.

Xiu, D., 2007. Efficient collocational approach for parametric uncertainty analysis. Commun. Comput. Phys. 2 (2), 293–309.

Xiu, D., Hesthaven, J., 2005. High-order collocation methods for differential equations with random inputs. SIAM J. Sci. Comput. 27 (3), 1118–1139.

Xiu, D., Karniadakis, G., 2002. The Wiener–Askey polynomial chaos for stochastic differential equations. SIAM J. Sci. Comput. 24, 619–644.